

## RESEARCH ARTICLE

## Real-space visualization of intercalated water phases at the hydrophobic graphene interface with atomic force microscopy

Zhi-Yue Zheng<sup>1,2,3,\*</sup>, Rui Xu<sup>1,2,\*</sup>, Kun-Qi Xu<sup>2</sup>, Shi-Li Ye<sup>2</sup>, Fei Pang<sup>1</sup>, Le Lei<sup>1</sup>, Sabir Hussain<sup>2,4</sup>,  
Xin-Meng Liu<sup>1</sup>, Wei Ji<sup>1</sup>, Zhi-Hai Cheng<sup>1,†</sup><sup>1</sup>Beijing Key Laboratory of Optoelectronic Functional Materials & Micro-nano Devices, Department of Physics, Renmin University of China, Beijing 100872, China<sup>2</sup>CAS Key Laboratory of Standardization and Measurement for Nanotechnology, CAS Center for Excellence in Nanoscience, National Center for Nanoscience and Technology, Beijing 100190, China<sup>3</sup>State Key Laboratory of Digital Manufacturing Equipment and Technology, Department of Instrument Science and Technology, School of Mechanical Science and Engineering, Huazhong University of Science and Technology, Wuhan 430074, China<sup>4</sup>University of Chinese Academy of Sciences, Beijing 100039, China  
Corresponding author. E-mail: † zhihaicheng@ruc.edu.cn

Received June 14, 2019; accepted September 29, 2019

The phase behavior of water is a topic of perpetual interest due to its remarkable anomalous properties and importance to biology, material science, geoscience, nanoscience, etc. It is predicted confined water at interface can exist in large amounts of crystalline or amorphous states. However, the experimental evidence of coexistence of liquid water phases at interface is still insufficient. Here, a special folding few-layers graphene film was elaborate prepared to form a hydrophobic/hydrophobic interface, which can provide a suited platform to study the structure and properties of confined liquid water. The real-space visualization of intercalated water layers phases at the folding interface is obtained using advanced atomic force microscopy (AFM). The folding graphene interface displays complicated internal interfacial characteristics. The intercalated water molecules present themselves as two phases, low-density liquid (LDL, solid-like) and high-density liquid (HDL, liquid-like), according to their specific mechanical properties taken in two multifrequency-AFM (MF-AFM) modes. Furthermore, the water molecules structural evolution is demonstrated in a series of continuous MF-AFM measurements. The work preliminary confirms the existence of two liquid phases of water in real space and will inspire further experimental work to deeply understanding their liquid dynamics behavior.

**Keywords** 2D material, interfacial intercalation, coexistence of liquid water phases, multifrequency-AFM, hydrophobic graphene interface

## 1 Introduction

Water is one of the most anomalous liquids, whose anomalies become most evident in the supercooled state at sub-zero temperatures. It has been postulated that water can exist as two distinct, ultraviscous liquids in the metastable supercooled regime, namely low- and high-density liquid water (LDL and HDL, respectively) [1]. Furthermore, it is hypothesized that the observed low- and high-density amorphous ice forms (LDA and HDA, respectively) are the glassy counterparts of the two liquid forms through the glass-liquid transition [2–7]. On the basis of the foregoing hypothesis and theory, optical microscopy [8] and spectroscopy studies [1, 9] demonstrate the existence of both low- and high-density liquid water and their transi-

tion, but real-space visualization of these two liquid water phases is still insufficient.

When the bulk water is confined at nanoscale, such as nanocapillary or interface, they do have different structural forms and dynamic behaviors from that of bulk water [10, 11]. The water layers confined between hydrophobic/hydrophilic interfaces under ambient conditions have been extensively studied by atomic force microscopy (AFM). AFM is an ideal tool to realize characterizations of both structure and local mechanical, electrical and thermal properties [12–15] at nanoscale, where MF-AFM is extremely sensitive to dissipation of sample [16–18]. At hydrophobic/hydrophilic interfaces, water layers show the ice-like structure of one [19–24] or two puckered bilayers [19–21, 25–28], whose electrical and thermal properties have also been well studied. However, the liquid phase of confined water still needs further investigation.

\*These authors contributed equally to this work.

Hydrophobic/hydrophobic interface, such as graphene/graphene interface, can provide a platform to study the liquid phase of confined water [29–31]. Liquid-like nanodroplets (10–100 nm) can be easily observed at step edges and surface defects with the help of graphene coating. Algara-Siller *et al.* [32, 33] recently demonstrated that when water is constrained between two sheets of graphene, it becomes a two-dimensional (2D) liquid and has an intriguing monolayer solid with a square pattern under van der Waals pressure. Although several simulations [21, 34, 35] works about the water constrained at hydrophobic/hydrophobic interface arise after that, the direct experimental evidence of two liquid water phases at hydrophobic/hydrophobic interface still need insight investigation.

Here, a special folding few-layers graphene film was elaborately prepared [Fig. 1(a)] to form a hydrophobic/hydrophobic interface, which can provide a suited platform to study the structure of confined liquid water. The real-space visualization of liquid phases of intercalated water and their evolution at folding graphene interface are obtained using advanced-AFM. Domains/boundaries-like characteristics were observed at the folding interface of graphene films in friction force microscopy (FFM) [36], which cannot be observed in topography. In order to realize the intercalation of water molecules, we precool the sample with a constant temperature and humidity equipment for several hours [Fig. 1(b)]. Then we put the sample in a warm and high humidity condition to realize the H<sub>2</sub>O intercalating the whole hydrophobic/hydrophobic interface for a long enough time,

as shown in Fig. 1(c). Because the amplitude ( $A_{MF}$ ) of MF-AFM can reflect the local mechanical properties of the sample and has subsurface detection capability [Fig. 1(d)] [37], the internal interfacial intercalation water phases were further visualized with two MF-AFM modes: multiharmonic AFM and dual AC AFM mode. Both the low-density liquid (LDL, solid-like) and high-density liquid (HDL, liquid-like) water phases were clearly observed in these MF-AFM signal channels due to their specific mechanical properties. Among the confined water films, the dynamic structural evolution between LDL and HDL were further illustrated in time-series MF-AFM measurements. In contrast to the unobvious structural evolution observed in the passive MF-AFM (multiharmonic) mode, the prominent structure evolution was observed in the active MF-AFM (dual AC) mode due to the relative strong tip-sample interaction forces.

## 2 Materials and methods

The graphene flake is deposited in ambient condition by mechanically exfoliating commercially graphite crystal (HQ Graphene from Netherlands) onto the SiO<sub>2</sub>/Si substrate using the normal scotch-tape micromechanical cleavage method. The prepared sample has been systematically investigated in dry air for several days and it has been left unchanged, which imply air molecules are hard to be intercalated at interface.

Then, the sample was precooled at 5° and relative

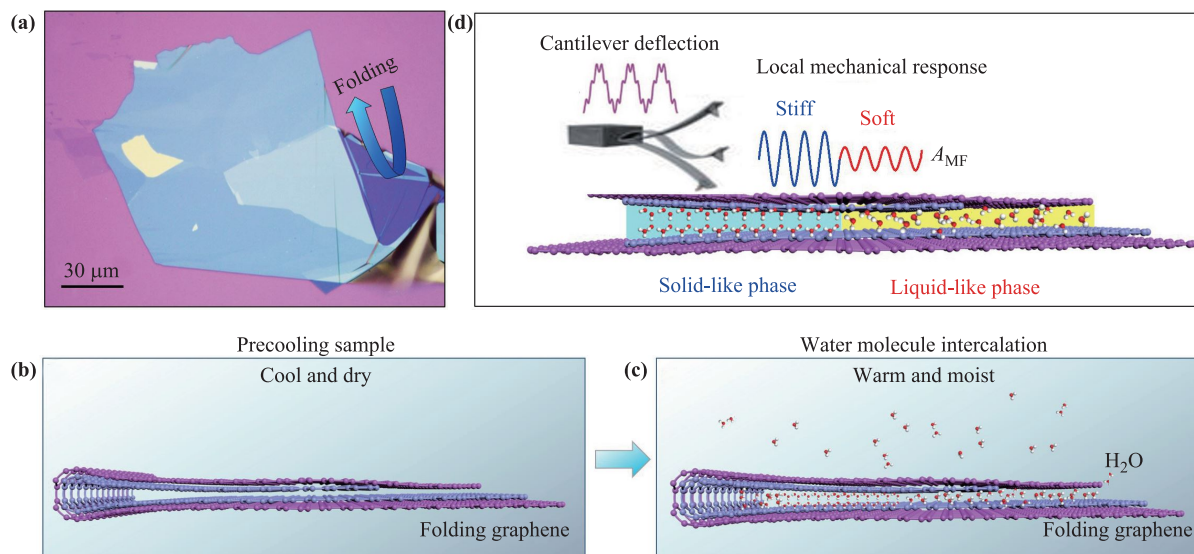


**Fig. 1** Water molecule intercalation at folding few-layers graphene sheet. (a) Bright-field optical microscope image of the mechanically exfoliated folding few-layers graphene flake on SiO<sub>2</sub>/Si substrate. It has advantages in encapsulating water molecules because of its mechanical strength and chemical stability [33]. (b) Side-view of folding graphene. Internal decoupling interface between two sheets is formed. (c) Model of water molecule intercalation at the interface of folding graphene. (d) The basic principle of MF-AFM. The amplitude ( $A_{MF}$ ) of MF-AFM can reflect the local mechanical properties (elastic modulus, viscoelasticity and etc.) of sample and has subsurface detection capability. The different phase structures of intercalated water layers are expected to be observed by MF-AFM.

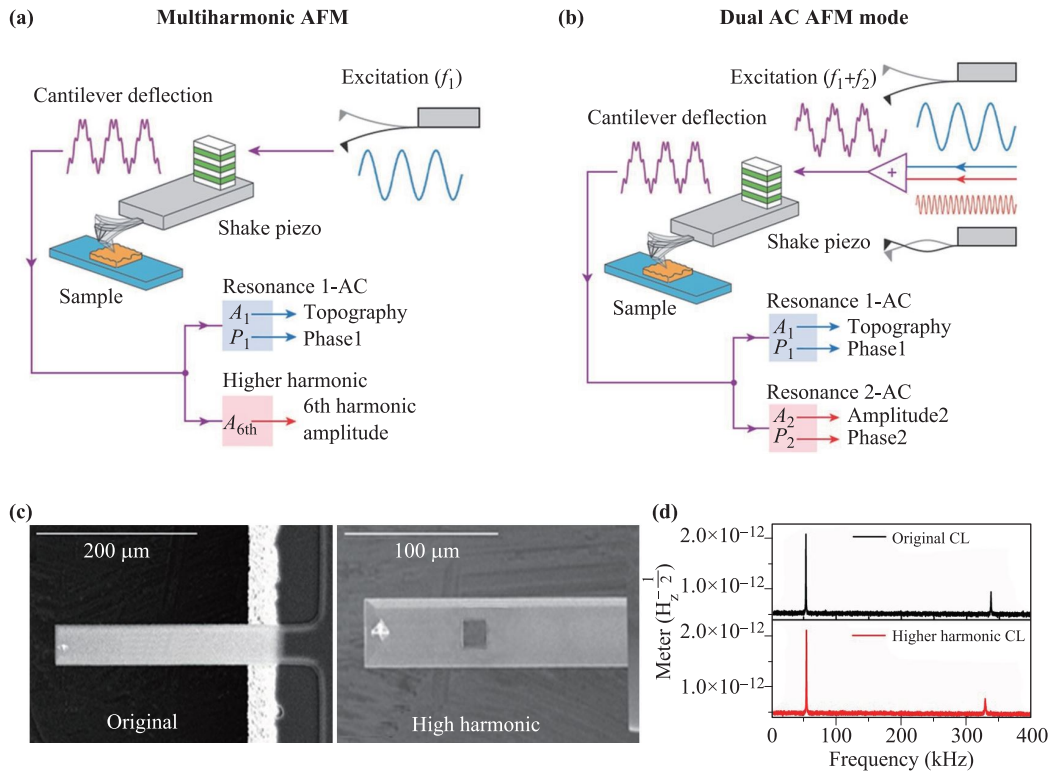


**Fig. 2** Schematic diagrams of advanced atomic force microscopy. **(a)** Schematic of the multiharmonic AFM mode. Only driving the cantilever at its first resonance mode, meanwhile recording the higher harmonic components introduced by the nonlinearity of the tip-sample interaction forces during the conventional dynamic AFM imaging. **(b)** Schematic of the dual AC AFM mode. The cantilever is simultaneously driven at two of its eigenmodes (resonant modes), and the amplitude and phase of two eigenmodes are recorded. **(c)** The scanning electron microscopy (SEM) images of the original and 6th harmonic probes. **(d)** The frequency response spectroscopy of the original and 6th harmonic cantilever (CL) obtained with the thermal noise spectrum measurement.

humidity (RH) ~5% for several hours and then placed in moist and relatively high temperature environments. Hence H<sub>2</sub>O molecules intercalate into the interface. In order to realize H<sub>2</sub>O molecules intercalating the whole hydrophobic/hydrophobic interface, the folding graphene has been placed in the high humidity condition (relative humidity > 90%) for several days. Furthermore, the interface dewetting process would not occur when the water intercalated folded graphene placed in a dry environment. This provides us a platform to investigate the confined water in hydrophobic/hydrophobic interface.

All AFM measurements were carried out on a commercial AFM (MFP-3D Infinity, Asylum Research) under ambient environment. The FFM is performed by simply adjusting the fast scanning direction of AFM probe while keeping the sample fixed. The scan angle is defined as the relative angle between scan direction and the long axis of

the cantilever [38, 39]. Except FFM, we employ the MF-AFM to investigate the water intercalated sample, which is based on the excitation and/or detection of several frequencies of the probe’s oscillation simultaneously. Specifically, two kinds of multi-frequency modes are employed to study the intercalated water at interface: multiharmonic mode and dual AC mode, which has enhanced contrast and sensitivity for mapping conservative and dissipative nanoscale heterogeneity [13, 40, 41]. The multiharmonic mode is the most straightforward MF-AFM mode, shown as Fig. 2(a). It is only driven at first resonance mode of cantilever. Meanwhile requires the recording of the higher harmonic components introduced by the nonlinearity of the tip-sample interaction forces during the conventional dynamic AFM imaging. (See details in Supplementary Materials) In amplitude-modulation AFM, the amplitude of higher harmonics can be expressed as [16–18]

$$A_n = S \frac{\omega_0}{k} \sqrt{\left( \int_0^T F_{ts}(d) \cos(n\omega t) dt \right)^2 + \left( \int_0^T F_{ts}(d) \sin(n\omega t) dt \right)^2}, \tag{1}$$

$$S \approx \frac{1}{\pi n^2}, \quad n > 3, \tag{2}$$

where  $F_{ts}$  represents the tip-surface force;  $d$  is the instantaneous tip-surface separation;  $\omega_0$  is the fundamental resonant frequency;  $A_n$  is the amplitude of the  $n$ -th harmonic with angular frequency  $n\omega$  and is related to elastic modules. The theoretical analysis [Eqs. (1)–(2)] shows that the amplitude of the high harmonics decreases with the order as  $\sim 1/n^2$ , which means the harmonic amplitude is too weak to detect with the conventional dynamic AFM cantilever. Therefore, the special harmonic cantilever is designed, fabricated and used here [Figs. 2(c, d)], which allowed the tuning of its second eigenmode coincidence with the 6 times of the first eigenmode to increase the signal to noise level. Hence, the harmonic amplitude abbreviated as  $A_{6th}$  here.

The dual AC mode is another multi-frequency mode that uses two eigenmode frequencies of AFM cantilever. In this mode, the cantilever is simultaneously driven at two of its eigenmodes (resonant modes), as shown in Fig. 2(b). The first resonance mode of cantilever operates the same as regular amplitude modulation mode (i.e., tapping mode). Additionally, the second resonance mode works without any feedback and its amplitude ( $A_2$ ) and phase ( $P_2$ ) response are recorded. The total energy dissipated per cycle  $E_{dis}$  can be approximated as the sum of the contribution from the two eigenmodes:

$$\begin{aligned}
 E_{dis} &\approx E_{dis}(1) + E_{dis}(2) \\
 &= \frac{\pi k_1 A_{01} A_1}{Q_1} \left( \sin \phi_1 - \frac{A_1}{A_{01}} \right) \\
 &\quad + \frac{n\pi k_2 A_{02} A_2}{Q_2} \left( \sin \phi_2 - \frac{A_2}{A_{02}} \right), \quad (3)
 \end{aligned}$$

where  $Q_i$ ,  $k_i$ , and  $A_{0i}$  are the quality factor, force constant, free amplitude, respectively, of the  $i$ th eigenmode. Equation (3) links the second modal observables with non-conservative interactions ( $E_{dis}$ ). Under the same experimental conditions, the higher  $A_2$  is, the smaller dissipation is.

The silicon AFM probes (AC240, Asylum Research) were used in FFM and dual AC mode, which typically have specific tip radius  $R \sim 7$  nm, force constant  $k \sim 2.0$  N/m, and the resonance frequency of first resonance mode  $f_{r1} \sim 76.3$  kHz and second resonance mode  $f_{r2} \sim 451.4$  kHz. In multiharmonic mode, a special harmonic cantilever is designed, fabricated and used at here [Figs. 2(c, d) and Fig. S1 of Supplementary Materials]. The home-made 6th harmonic AFM probe was home-made by modified the original rectangular AFM cantilever (STG55N, tjlvtiao) with focused ion beam (FIB).

### 3 Results

Figures 3(a) and (b) show the topography and friction images of the selected area of the folding few-layers graphene flake. It is noted that the friction image shows complicated internal features (i.e., curved domain boundaries), while no apparent corresponding features are observed in the topography image. These different internal features are further clearly shown in the close-up friction images [Figs. 3(d, e) and S3], which are marked in Fig. 3(c). Figure 3(f) shows the line profiles of the trace and retrace scans along the dashed lines in Figs. 3(d) and (e). Con-

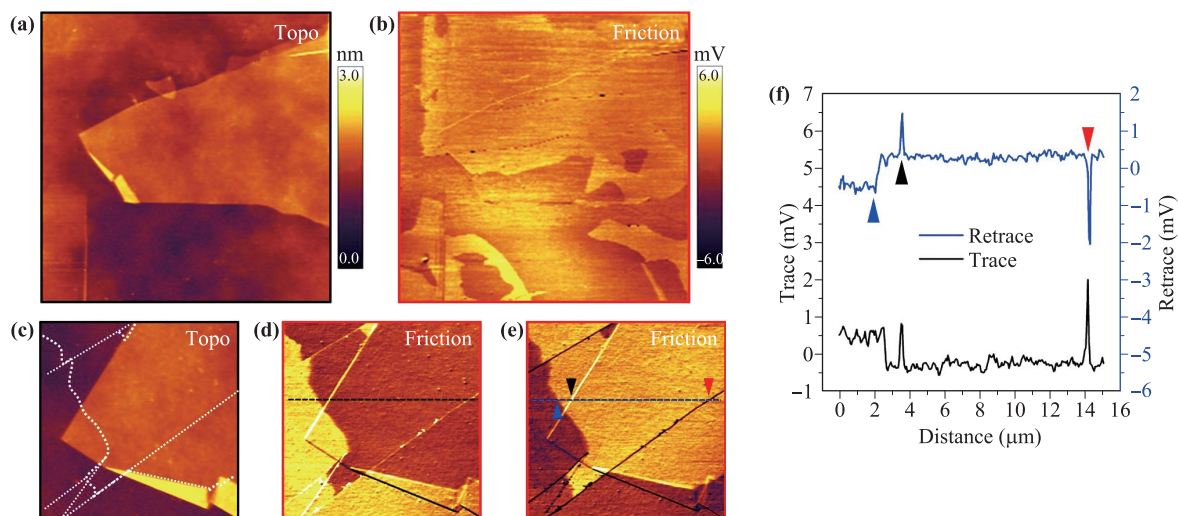


**Fig. 3** Friction force microscopy visualization of the internal folding graphene interface. (a, b) Topography and corresponding friction images. Complicated internal interfacial characteristics are visible in the friction images, but not observed in the topography image. Scan size:  $60 \mu\text{m}$ . (c–e) The simultaneously obtained close-up (c) topography, (d) friction trace and (e) friction retrace images. Internal interfacial “domain-/boundary-like” characteristics are highlighted in (c), which revealed in the friction images (d, e). Scan size:  $15 \mu\text{m}$ . (f) The section lines along dash lines in (d, e). A topologically visible surface step is indicated by black marker; the topologically invisible domain boundaries and straight-line features are indicated by blue and red markers.

sidering the friction force contrast dependent on thickness (i.e., number) of 2D layers and their interface adhesion (i.e., bonding), the features marked by the white lines in Fig. 3(c) result from the complicated interfacial structures of the folding interface formed during the mechanical exfoliation.

The above folding few-layers graphene provides an interface between two hydrophobic surfaces, which is a suitable platform to investigate the liquid phase of water. To control the H<sub>2</sub>O molecules intercalation into the interface, the sample was firstly precooled and then detected by AFM. Sequential AFM topography and friction images (Fig. S4) during the intercalation process were measured.

In order to realize H<sub>2</sub>O molecules intercalating the whole hydrophobic/hydrophobic interface, the folding graphene has been placed in the high humidity condition (relative humidity > 90%) for several days. It is certified that the interface is all full of liquid or solid water, other than air bubbles. The topography of folding graphene after water intercalation is shown in Fig. 4(a), which has no

obvious difference from the pristine sample. Considering MF-AFM can detect the subsurface mechanical properties and provide higher spatial resolution, we employ the MF-AFM to investigate the water intercalated sample [16–18, 42].

Thanks to the subsurface information obtained through nanomechanical coupling between tip and sample, two kinds of water phases can be distinguished obviously through the MF-AFM detection [Fig. 4(b)]. According to the value of  $A_{MF}$ , the water phase which has smaller  $A_{MF}$  [darker contrast in Fig. 3(b)] is named as  $WP_{MF-small}$ , and the other one (brighter contrast) is called  $WP_{MF-large}$ . The water phase  $WP_{MF-small}$  basically has separated circular or elliptical structure, which is indicated by the dark blue marker in Fig. 4(c). Meanwhile, the water phase  $WP_{MF-large}$  is full of the remaining space of graphene interface. Additionally, when  $WP_{MF-small}$  gathered around internal features [domain boundaries or steps at interface, which are marked by the guide line in Fig. 4(c) and arrows in Fig. 4(d)], it shows a semi ellipse-like shape (light blue

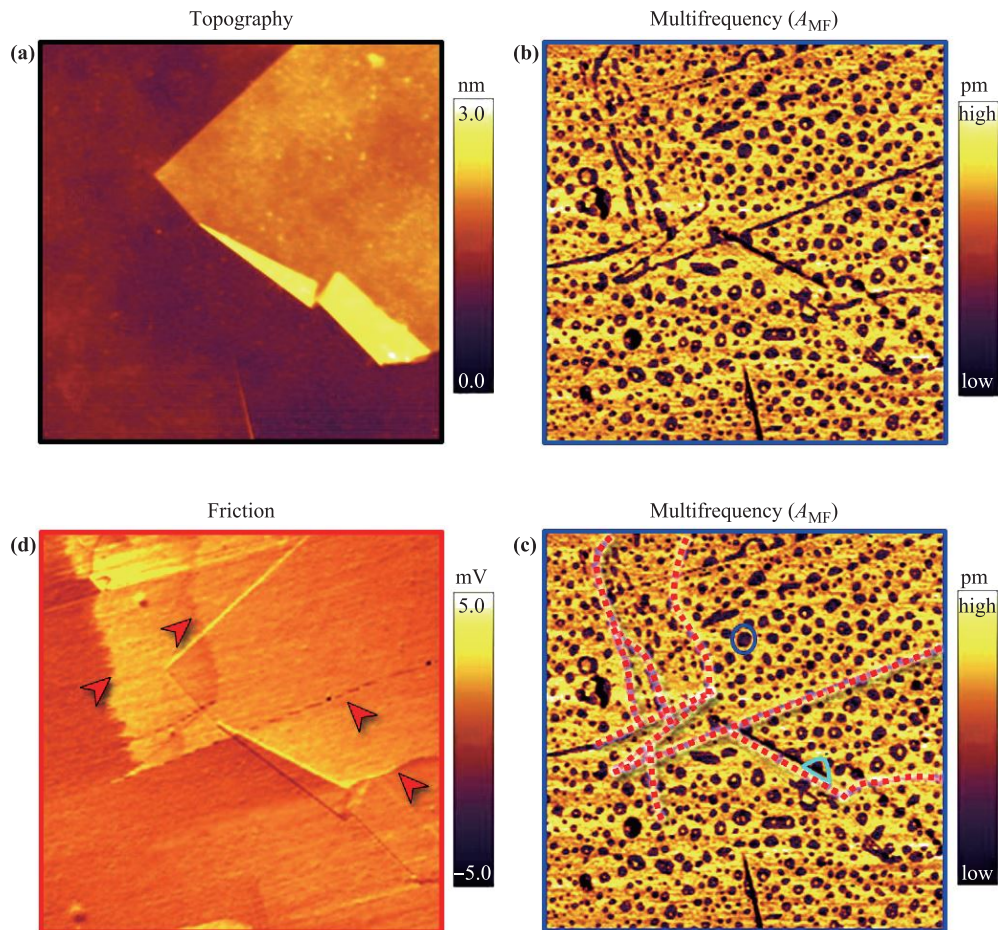


**Fig. 4** Multifrequency-AFM visualization of the intercalated water structures. (a, b) The AFM topography and amplitude of MF-AFM ( $A_{MF}$ ) of water intercalated sample taken in dual AC mode. There are two water phases coexist at interface, named as  $WP_{MF-small}$  and  $WP_{MF-large}$  here according to the value of  $A_{MF}$ . (c) The same  $A_{MF}$  image as (b). “Domain-/boundary-like” features at folding graphene interface which can affect the distribution of water phases are plotted in it. (d) The friction force image, where the internal features (domain boundaries or steps at interface) are marked by red arrows. Scan size: 25  $\mu\text{m}$ .

marker). It means the distribution of these two phases is affected by the internal interfacial structures. This also confirms the water layers are intercalated at interface, but not surface of sample.

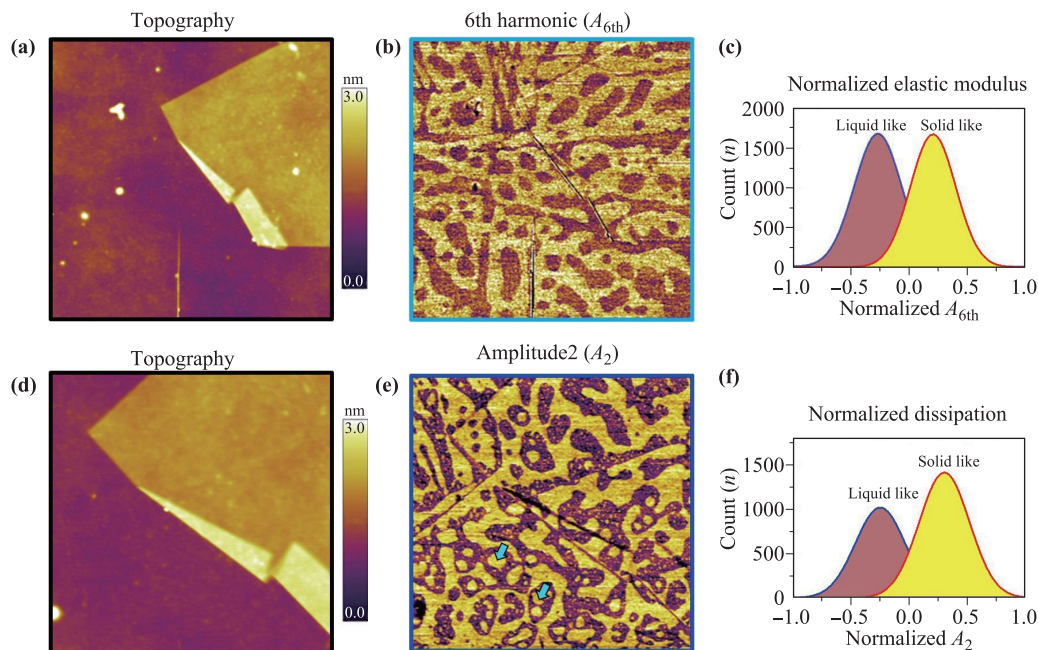
Figures 5(a) and (b) are the topography and the higher harmonic  $A_{6\text{th}}$  images of water intercalated sample obtained in multiharmonic mode. According to the above theoretical analysis [13], the higher  $A_{6\text{th}}$  (brighter contrast) is, the larger elastic modulus is. The corresponding histogram in Fig. 5(c), which is extracted from Fig. 5(b), reveals that two kinds of water structure are coexistence between the two hydrophobic surfaces. The larger elastic modulus areas, which corresponding to the brighter areas in  $A_{6\text{th}}$  image, are representative of the “solid-like” phase of the intercalation water layers. On the contrary, the smaller elastic modulus areas (dark areas in  $A_{6\text{th}}$ ) indicate “liquid-like” phase region.

Figure 5(e) shows the  $A_2$  images of the water intercalated sample. Histogram distribution of  $A_2$  extracted from Fig. 5(e) are shown in Fig. 5(f). It also displays two kinds of water structure are coexistence at the folding graphene interface. From the above theory, the higher  $A_2$  (brighter contrast) indicate the strong repulsive (rigid) and less dissipated tip-sample forces, so the bright areas should be the “solid-like” phase. The dark areas with lower  $A_2$  are “liquid-like” phase considering their soft and dissipative nature.

Generally, both experimental data of multiharmonic mode ( $A_{6\text{th}}$ ) and dual AC mode ( $A_2$ ) demonstrate the “solid-like” and “liquid-like” water phases coexist at in-

terface. The “solid-like” and “liquid-like” layer always affected by the internal interfacial structures, which confirm the water layers are intercalated at interface. On the other hand, there are detailed structural differences between them. The distribution rates of “solid-like” and “liquid-like” water phases are almost same in  $A_{6\text{th}}$  image. However, in the  $A_2$  image, the distribution rates are  $\sim 60\%$  for “solid-like” and  $\sim 40\%$  for “liquid-like” phases. This discrepancy results from the tip-sample interaction difference in two MF-AFM modes. Tip-sample force is weaker in multiharmonic mode (passive MF-AFM mode) than that in dual AC mode (active MF-AFM mode). The relative stronger tip-sample interaction in dual AC mode also results in small round solid-like phase islands were observed within the liquid-like phase in  $A_2$  images [indicated by arrows in Fig. 5(e)]. Besides, the tip-sample interaction difference further resulting in the dynamic evolution of water phases are different in these two MF-AFM modes, which are presented in Fig. 6.

Figures 6(a–c) show the time-series snapshots of  $A_{6\text{th}}$  images. No prominent but few unobvious structural changes are observed in multiharmonic mode (passive MF-AFM mode). We extract the coverage percentage of liquid-like phases and plotted in Fig. 6(d). It shows the coverage of two water phases are almost same and basically does not change with time in the multiharmonic mode. What's more, the structural evolution of water layers under dual AC mode is also studied. Both the overall and detailed structure of solid-like and liquid-like phases changing can clearly be seen in Figs. 6(e–g). The coverage of two liquids



**Fig. 5** Coexistence of solid-like and liquid-like phases. (a, b) The topography and  $A_{6\text{th}}$  image of water intercalated sample in multiharmonic mode. Scan size: 30  $\mu\text{m}$ . (c) Histogram distribution of  $A_{6\text{th}}$ /elastic modulus extracted from (b). Arbitrarily units (a.u.) are used here to qualitative description  $A_{6\text{th}}$ /elastic modulus of interfacial water layer. (d, e) The topography and  $A_2$  image of water intercalated sample taken in dual AC mode. Scan size: 15  $\mu\text{m}$ . (f) Histogram distribution of  $A_2$ /dissipation extracted from (e).

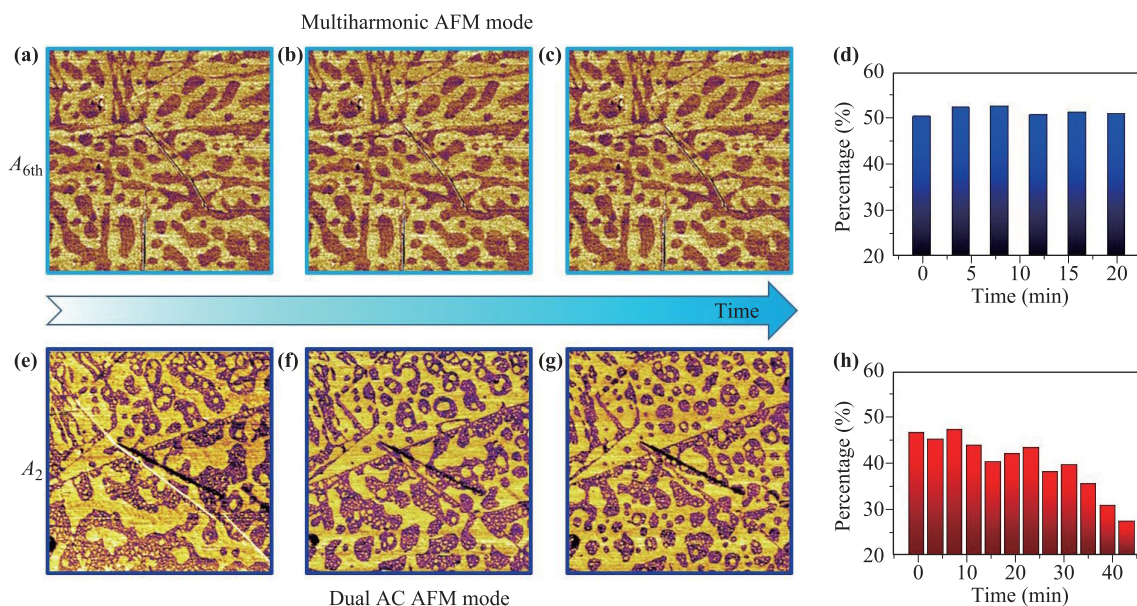


**Fig. 6** Multifrequency-AFM visualization of the intercalated water phases transition. (a–c) Series of  $A_{6th}$  images acquired with the same time interval  $\sim 7$  minutes. (d) The percentage of liquid-like phase changes with time in multiharmonic mode. (e–g) Series of  $A_2$  images acquired with the same time interval  $\sim 7$  minutes. (h) The percentage of liquid-like phase changes with time in dual AC mode. Scan size:  $30 \mu\text{m}$ .

phases changes obviously in the scanning process of dual AC mode [Fig. 6(h)]. The dynamic behavior of water layers in dual AC mode (active MF-AFM mode) is distinctly from that in multiharmonic mode, because the tip-sample interaction forces are different in these two modes. The phase transition here confirm the confined water layers at the folding graphene interface is not a single phase, and the exact structure of intercalated water will be shown in the discussion part.

## 4 Discussion and conclusion

Previous theoretical studies [21, 34] had predicted numerous crystalline and amorphous ice from simulations when water is confined in two parallel flat hydrophobic plates (such as graphene interface), which is dependent on the vertical size of the interface ( $h$ ), the vdW pressure ( $P_{vdW}$ ), and the temperature ( $T$ ). Zhu *et al.* [21] have reported a semi-quantitative phase diagram and phase transitions of 2D water molecules constrained in graphene interface changes with  $h$  and  $P_{vdW}$  at room temperature. In general, transition pressure from liquid phase to solid phase is increasing as the increase of  $h$ . For example, the transition pressure is  $\sim 600$  MPa for  $h = 0.6$  nm, while it is increased to  $\sim 2$  GPa when  $h$  is 1 nm. Normally, water constrained at graphene interface suffers van der Waals (vdW) pressure, which can be as high as 1 GPa. It means the liquid water layer can be confined at the folding interface of graphene because the interlayer distance of folding interface is large since the weak interlayer interaction at

the folding interface. Confined water can be viewed as a coexistence of monolayer, bilayer, and trilayer liquid domains to accommodate the inhomogeneous confinement at the folding interface at room temperature [43].

Among the liquid phase of water, there are two different phases which have different density, known as low-density liquid (LDL) and high-density liquid (HDL). Considering the fragility indices  $m = 14$  for the low-density and  $m = 20\text{--}25$  for the high-density liquid, LDL is a “superstrong” liquid and HDL is less strong than LDL [44].

Combing the analysis of multiharmonic data and above discussion, phases of liquid water have been determined through the value of elastic modulus. The water phase which has larger elastic modulus (solid-like phase) is LDL, while the other (liquid-like phase) is HDL. Importantly, the experimental evidences of  $A_{6th}$  confirm these two phases are both liquid water phases: first, the boundaries between two phases are curved lines, which are different from the edges of ice layer whose boundaries are straight and tend to have hexagonal shapes. Second, the separated liquid-like structures scattered in the solid-like liquid, which can be attribute to the larger cohesion of HDL comparing to LDL.

The distribution ratio of HDL and LDL obviously changes because the relatively strong tip-sample interaction (comparing to multiharmonic mode) during the dual AC scanning, which is indicated by previous work [1, 5]. Perakis *et al.* gave the evidence of LDL and HDL coexistence and transition at low temperature  $\sim 130$  K, and point to the existence of a first-order phase transition between HDL and LDL, which can exist at higher temper-

ature and under pressure. In our experiments, the transition between two phases is easy and locally reversible under the same scanning parameters at room temperature and high pressure ( $\geq P_{vdW}$ ). The easy phase transition confirm these two phases are both liquid phase of water.

Here, we have preliminarily verified the LDL and HDL phase exist and their transition at vdW interface at room temperature in real-space experiments, by using well-prepared folding graphene as our sample and employing the MF-AFM to detect the interface mechanical property of water layer. The phase transition still needs further experimental and simulation studies. We believe this work will inspire the researchers to deeply understanding the liquid dynamics behavior.

**Electronic supplementary material** Supplementary material is available in the online version of this article at <https://doi.org/10.1007/s11467-019-0933-0> and is accessible for authorized users.

**Acknowledgements** This project was supported by the Ministry of Science and Technology (MOST) of China (No. 2016YFA0200700), the National Natural Science Foundation of China (NSFC) (Nos. 21622304, 61674045, and 11604063), the Strategic Priority Research Program, the Key Research Program of Frontier Sciences and Instrument Developing Project of Chinese Academy of Sciences (CAS) (Nos. XDB30000000, QYZDB-SSW-SYS031, and YZ201418). Z. H. Cheng was supported by Distinguished Technical Talents Project and Youth Innovation Promotion Association CAS, the Fundamental Research Funds for the Central Universities and the Research Funds of Renmin University of China (No. 18XNLG01).

## References

1. F. Perakis, K. Amann-Winkel, F. Lehmkuhler, M. Sprung, D. Mariedahl, J. A. Sellberg, H. Pathak, A. Späh, F. Cavalca, D. Schlesinger, A. Ricci, A. Jain, B. Massani, F. Aubree, C. J. Benmore, T. Loerting, G. Grübel, L. G. M. Pettersson, and A. Nilsson, Diffusive dynamics during the high-to-low density transition in amorphous ice, *Proc. Natl. Acad. Sci. USA* 114(31), 8193 (2017)
2. C. U. Kim, M. W. Tate, and S. M. Gruner, Glass-to-cryogenic-liquid transitions in aqueous solutions suggested by crack healing, *Proc. Natl. Acad. Sci. USA* 112(38), 11765 (2015)
3. C. U. Kim, B. Barstow, M. W. Tate, and S. M. Gruner, Evidence for liquid water during the high-density to low-density amorphous ice transition, *Proc. Natl. Acad. Sci. USA* 106(12), 4596 (2009)
4. P. H. Poole, F. Sciortino, U. Essmann, and H. E. Stanley, Phase-behavior of metastable water, *Nature* 360(6402), 324 (1992)
5. J. C. Palmer, F. Martelli, Y. R. Liu, A. Z. Car, A. Z. Panagiotopoulos, and P. G. Debenedetti, Metastable liquid-liquid transition in a molecular model of water, *Nature* 510(7505), 385 (2014)
6. K. Amann-Winkel, R. Böhmer, F. Fujara, C. Gainaru, B. Geil, and T. Loerting, Water's controversial glass transitions, *Rev. Mod. Phys.* 88(1), 011002 (2016)
7. E. O. Rizzatti, M. A. A. Barbosa, and M. C. Barbosa, Core-softened potentials, multiple liquid-liquid critical points, and density anomaly regions: An exact solution, *Front. Phys.* 13(1), 136102 (2018)
8. O. Mishima, K. Takemura, and K. Aoki, Visual observations of the amorphous-amorphous transition in H<sub>2</sub>O under pressure, *Science* 254(5030), 406 (1991)
9. K. Winkel, E. Mayer, and T. Loerting, Equilibrated high-density amorphous ice and its first-order transition to the low-density form, *J. Phys. Chem. B* 115(48), 14141 (2011)
10. F. Martelli, H. Y. Ko, C. C. Borallo, and G. Franzese, Structural properties of water confined by phospholipid membranes, *Front. Phys.* 13(1), 136801 (2018)
11. V. De Michele, G. Romanelli, and A. Cupane, Dynamics of supercooled confined water measured by deep inelastic neutron scattering, *Front. Phys.* 13(1), 138205 (2018)
12. B. Bhushan, *Nanotribology, Nanomechanics, and Materials Characterization*, Chapter 28, 2011
13. B. Bhushan, *Springer Handbook of Nanotechnology*, 2010
14. K. Xu, S. Ye, L. Lei, L. Meng, S. Hussain, Z. Zheng, H. Zeng, W. Ji, R. Xu, and Z. Cheng, Dynamic interfacial mechanical-thermal characteristics of atomically thin two-dimensional crystals, *Nanoscale* 10(28), 13548 (2018)
15. R. Xu, S. Ye, K. Xu, L. Lei, S. Hussain, Z. Zheng, F. Pang, S. Xing, X. Liu, W. Ji, and Z. Cheng, Nanoscale charge transfer and diffusion at the MoS<sub>2</sub>/SiO<sub>2</sub> interface by atomic force microscopy: contact injection versus triboelectrification, *Nanotechnology* 29(35), 355701 (2018)
16. R. Garcia and E. T. Herruzo, The emergence of multi-frequency force microscopy, *Nat. Nanotechnol.* 7(4), 217 (2012)
17. R. Garcia, *Amplitude Modulation Atomic Force Microscopy*, Wiley-VCH Verlag GmbH & Co. KGaA, 2010
18. L. Tetard, A. Passian, and T. Thundat, New modes for subsurface atomic force microscopy through nanomechanical coupling, *Nat. Nanotechnol.* 5(2), 105 (2010)
19. J. I. Bai and X. C. Zeng, Polymorphism and polyamorphism in bilayer water confined to slit nanopore under high pressure, *Proc. Natl. Acad. Sci. USA* 109(52), 21240 (2012)
20. W. H. Zhao, L. Wang, J. Bai, L. F. Yuan, J. L. Yang, and X. C. Zeng, Highly confined water: Two-dimensional ice, amorphous ice, and clathrate hydrates, *Acc. Chem. Res.* 47(8), 2505 (2014)
21. Y. B. Zhu, F. C. Wang, J. I. Bai, X. C. Zeng, and H. A. Wu, Compression limit of two-dimensional water constrained in graphene nanocapillaries, *ACS Nano* 9(12), 12197 (2015)
22. R. Zangi and A. E. Mark, Monolayer ice, *Phys. Rev. Lett.* 91(2), 025502 (2003)
23. J. Bai, C. A. Angell, and X. C. Zeng, Guest-free monolayer clathrate and its coexistence with two-dimensional high-density ice., *Proc. Natl. Acad. Sci. USA* 107(13), 5718 (2010)

24. K. Koga, H. Tanaka, and X. C. Zeng, First-order transition in confined water between high-density liquid and low-density amorphous phases, *Nature* 408(6812), 564 (2000)
25. R. Zangi and A. E. Mark, Bilayer ice and alternate liquid phases of confined water, *J. Chem. Phys.* 119(3), 1694 (2003)
26. K. Koga, X. C. Zeng, and H. Tanaka, Freezing of confined water: A bilayer ice phase in hydrophobic nanopores, *Phys. Rev. Lett.* 79(26), 5262 (1997)
27. S. H. Han, M. Y. Choi, P. Kumar, and H. E. Stanley, Phase transitions in confined water nanofilms, *Nat. Phys.* 6(9), 685 (2010)
28. H. Lee, J. H. Ko, J. S. Choi, J. H. Hwang, Y. H. Kim, M. Salmeron, and J. Y. Park, Enhancement of Friction by Water Intercalated between Graphene and Mica, *J. Phys. Chem. Lett.* 8(15), 3482 (2017)
29. K. S. Novoselov, D. V. Andreeva, W. Ren, and G. Shan, Graphene and other two-dimensional materials, *Front. Phys.* 14(1), 13301 (2019)
30. R. Wang, X. G. Ren, Z. Yan, L. J. Jiang, W. E. I. Sha, and G. C. Shan, Graphene based functional devices: A short review, *Front. Phys.* 14(1), 13603 (2019)
31. S. Hussain, K. Xu, S. Ye, L. Lei, X. Liu, R. Xu, L. Xie, and Z. Cheng, Local electrical characterization of two-dimensional materials with functional atomic force microscopy, *Front. Phys.* 14(3), 33401 (2019)
32. Q. Li, J. Song, F. Besenbacher, and M. D. Dong, Two-dimensional material confined water, *Acc. Chem. Res.* 48(1), 119 (2015)
33. G. Algara-Siller, O. Lehtinen, F. C. Wang, R. R. Nair, U. Kaiser, H. A. Wu, A. K. Geim, and I. V. Grigorieva, Square ice in graphene nanocapillaries, *Nature* 519(7544), 443 (2015)
34. Y. Zhu, F. Wang, J. Bai, X. C. Zeng, and H. Wu, AB-stacked square-like bilayer ice in graphene nanocapillaries, *Phys. Chem. Chem. Phys.* 18(32), 22039 (2016)
35. J. Chen, G. Schusteritsch, C. J. Pickard, C. G. Salzmann, and A. Michaelides, Two dimensional ice from first principles: Structures and phase transitions, *Phys. Rev. Lett.* 116(2), 025501 (2016)
36. J. S. Choi, J. S. Kim, I. S. Byun, D. H. Lee, M. J. Lee, B. H. Park, C. Lee, D. Yoon, H. Cheong, K. H. Lee, Y. W. Son, J. Y. Park, and M. Salmeron, Friction anisotropy-driven domain imaging on exfoliated monolayer graphene, *Science* 333(6042), 607 (2011)
37. Z. Zheng, R. Xu, S. Ye, S. Hussain, W. Ji, P. Cheng, Y. Li, Y. Sugawara, and Z. Cheng, High harmonic exploring on different materials in dynamic atomic force microscopy, *Sci. China Technol. Sci.* 61(3), 452 (2017)
38. K. Xu, Y. Pan, S. Ye, L. Lei, S. Hussain, Q. Wang, Z. Yang, X. Liu, W. Ji, R. Xu, and Z. Cheng, Shear anisotropy-driven crystallographic orientation imaging in flexible hexagonal two-dimensional atomic crystals, *Appl. Phys. Lett.* 115(6), 063101 (2019)
39. S. Ye, K. Xu, L. Lei, S. Hussain, F. Pang, X. Liu, Z. Zheng, W. Ji, X. Shi, R. Xu, L. Xie, and Z. Cheng, Nanoscratch on single-layer MoS<sub>2</sub> crystal by atomic force microscopy: Semi-circular to periodical zigzag cracks, *Mater. Res. Express* 6(2), 025048 (2018)
40. D. Martinez-Martin, E. T. Herruzo, C. Dietz, J. Gomez-Herrero, and R. Garcia, Noninvasive protein structural flexibility mapping by bimodal dynamic force microscopy, *Phys. Rev. Lett.* 106(19), 198101 (2011)
41. J. R. Lozano and R. Garcia, Theory of phase spectroscopy in bimodal atomic force microscopy, *Phys. Rev. B* 79(1), 014110 (2009)
42. Y. Li, C. Yu, Y. Gan, P. Jiang, J. Yu, Y. Ou, D. F. Zou, C. Huang, J. Wang, T. Jia, Q. Luo, X. F. Yu, H. Zhao, C. F. Gao, and J. Y. Li, Mapping the elastic properties of two-dimensional MoS<sub>2</sub> via bimodal atomic force microscopy and finite element simulation, *npj Comput. Mater.* 4(1), 49 (2018)
43. H. Qiu, X. C. Zeng, and W. Guo, Water in inhomogeneous nanoconfinement: Coexistence of multi layered liquid and transition to ice nanoribbons, *ACS Nano* 9(10), 9877 (2015)
44. K. Amann-Winkel, C. Gainaru, P. H. Handle, M. Seidl, H. Nelson, R. Bohmer, and T. Loerting, Water's second glass transition, *Proc. Natl. Acad. Sci. USA* 110(44), 17720 (2013)